A stabilized phase-field method for two-phase flow at high Reynolds number and large density/viscosity ratio

Zhicheng Wang [a,*], Suchuan Dong [b], Michael S. Triantafyllou [a],
Yiannis Constantinides [c], George Em Karniadakis [d]

[a] *Massachusetts Institute of Technology, Cambridge, MA 02139, USA*
[b] *Purdue University, West Lafayette, IN 47907, USA*
[c] *Chevron Energy Technology Company, Houston, TX 77002, USA*
[d] *Brown University, Providence, RI 02912, USA*

ARTICLE INFO

ABSTRACT

Simulating two-phase flows in realistic industrial-complexity conditions remains an open problem. We present a phase-field method based on the Cahn-Hilliard equation that is able to simulate two-phase flow at high Reynolds number and at large density and viscosity ratios. We employ the entropy-viscosity method (EVM), applied both on the Navier-Stokes equations and phase-field equation, to stabilize the simulation in conjunction with an EVM-based artificial interface compression method (AICM) that maintains the sharpness of the interface. We implement this method based on a hybrid spectral-element/Fourier (SEF) discretization and demonstrate second-order accuracy in time and spectral convergence rate in space for smoothed fabricated solutions. We first test the accuracy and robustness of the stabilized SEF-EVM solver by solving the so-called three-dimensional "LeVeque problem" and compare against other available methods. Subsequently, we simulate a rising air bubble in a water container and find that the method is robust with respect to various parameters of the phase-field formulation. Lastly, we apply the method to simulate the onset and subsequent evolution of an air/oil slug in a long horizontal pipe using realistic parameters and incorporating gravity and surface tension effects. This is a particularly difficult flow to simulate with existing methods in realistic conditions and here we show that the new stabilized phase-field methods yields results in good agreement with the experimental data.

© 2019 Elsevier Inc. All rights reserved.

1. Introduction

Two-phase flows are of great interest in many industrial applications such as oil and gas production, cooling of nuclear reactors, boiling and condensation in power plants, and fuel oil atomization in engines. Despite the development of several Eulerian and Lagrangian numerical methods and the still rapidly increasing computational speeds, the numerical simulation of two-phase flows in realistic conditions is an open challenge as it requires resolution of extremely unsteady, irregular and multiscale flow motions as well as frequent interface topology (non-smooth) changes. Specifically, difficulties in the simu-

lation are due, but are not limited to: (1) accurately describing the complex interface morphology; (2) achieving numerical stability in simulating two-phase flow at large density ratio and high Reynolds number; and (3) overcoming the computing bottleneck caused by the required highly resolved mesh. Currently, there are three widely used (Eulerian) methods that have attempted to tackle these difficulties, namely the volume of fluid (VoF) method, the level-set method, and the phase-field method. The VoF method is very popular in the engineering community, as it has clear physical interpretation and good mass conservation properties, but in principle, the marker function of the VoF method is a discontinuous field, thus an interface reconstruction step, such as the piece-wise linear interface construction [1,2] is necessary to obtain accurate approximations of interface curvature and normal direction. We note that for the VoF method in OpenFoam, an interface compression technique [3,4] is employed to maintain the sharpness of the interface, instead of interface reconstruction. The level-set method uses a continuous signed distance function as the marker to distinguish different fluids. One of the appealing advantages of the level-set method is that no additional procedure is required to compute the interface curvature and normal direction. However, in practice, the level-set function has to be re-initialized [5–7] every once in a while in order to maintain the so-called property of "signed distance". Moreover, the level-set method suffers considerably from the problem of losing mass and usually an explicit mass correction step is necessary [7]. Note that the conservative level-set method [8,9] and coupled level-set volume of fluid (CLSVOF) [10] method are also proposed to address the issue of mass conservation.

Conventionally, the above two methods are regarded as sharp interface methods, although the sharpness of the interface may be lost due to numerical effects, e.g., if the continuum surface force (CSF) is involved, which re-distributes the surface tension to a surrounding fluid. Nonetheless, in this paper, our interest is in the phase-field method. In contrast to the sharp interface approaches, here a diffuse interface is developed with nonzero thickness to connect the two immiscible fluids. A particularly attractive feature of the phase-field method is that the governing equations are derived from an energy variational approach, which leads to well-posed nonlinear coupled systems consistent with the thermodynamic laws [11]. Among the different formulations of the phase-field method, the Cahn-Hilliard approach is most popular since it has the intrinsic property of conserving mass [12] and it has been verified by numerical experiments of two phase fluids with different densities [11]. In particular, [13] proposed an efficient time-stepping scheme for the coupled incompressible Navier-Stokes and Cahn-Hilliard equations, which is proved numerically to be suitable for problems with density ratio up to 1 000. However, as was pointed out in a recent review [14], there are no reports on the application of the phase-field method to realistic and industrial scale two-phase flows. For the realistic two-phase flow, the challenge is not only limited to large density ratio, but is also associated with high Reynolds number, as the combined effect of the two makes the simulation extremely difficult to stabilize for codes that use explicit or semi-implicit time marching schemes, which are very common in direct numerical simulation (DNS) and large-eddy simulation (LES). Hence, in the current work, we introduce the so-called entropy-viscosity method (EVM) proposed by [15,16] to control such explosive numerical instabilities. We note that EVM can be also regarded as a promising subgrid eddy viscosity model for LES, as has been demonstrated recently by systematic numerical experiments of single phase turbulent flows [17,18]. In this paper, our attention is to apply the phase-field method to the simulation of the two-phase slug flow in a circular pipe, which is one of the most complex two-phase flow patterns in fluid dynamics [19,20]. We note that there are several other popular methods, e.g., the marker-and-cell method [21], the front tracking method [22] and the two-fluid method [23], but these methods are either suitable to particular type of two phase flow or impractical for realistic applications. As a final note, we would like to mention that [7] (section 6.2) gives a theoretical prof that the formula of surface tension term in the phase-field method is equivalent to the CSF approach in the VoF or level-set methods.

The rest of the paper is organized as follows: in section 2 we will present the algorithms to solve the coupled Navier-Stokes Cahn-Hilliard equations in the framework of the spectral-element/Fourier (SEF) discretization. In the same section, we will also propose the EVM with the associated AICM. In section 3, we test the convergence rate, and present the three-dimensional LeVeque problem and another benchmark, i.e., a rising air bubble in a water container. In section 4, we apply our method to simulate slug initiation and propagation in a horizontal pipe of 54 mm diameter and 4 m length using realistic parameters.

2. Mathematical models and numerical methods

2.1. Governing equations

In this paper, we consider the phase-field approach introduced by [13] for incompressible flows of gas/liquid, i.e., two immiscible fluids, which are governed by the following coupled system of equations,

$$\frac{\partial \mathbf{u}}{\partial t} + \mathbf{u} \cdot \nabla \mathbf{u} = -\frac{\nabla p}{\rho} + \frac{\mu}{\rho}\nabla^2 \mathbf{u} + \frac{\nabla \mu}{\rho} \cdot (\nabla \mathbf{u} + \nabla \mathbf{u^T}) - \frac{\lambda}{\rho}(\nabla^2\phi)\nabla\phi + \frac{\mathbf{f}(\mathbf{x},t)}{\rho} + \nabla \cdot (\nu_E \nabla \mathbf{u}), \quad (1)$$

$$\nabla \cdot \mathbf{u} = 0, \quad (2)$$

$$\frac{\partial \phi}{\partial t} + \mathbf{u}\cdot\nabla\phi = -\lambda\gamma_1\nabla^2\left[\nabla^2\phi - h(\phi)\right] + \nabla \cdot (C_\phi \nabla\phi). \quad (3)$$

In the above equations, $\mathbf{u}(\mathbf{x}, t)$ is velocity, $p(\mathbf{x}, t)$ is pressure, and $\mathbf{f}(\mathbf{x}, t)$ is a body force (mainly gravity in this paper), where $\mathbf{x}$ is the spatial coordinate and t is time, also ν_E is the so called entropy-viscosity; the detailed formulas will be given in section 2.2. Here $\phi(\mathbf{x}, t)$ is the so-called phase-field variable, whose value varies continuously in a range $[-1, 1]$ over the whole computational domain Ω. The region of $\phi = 1$ and $\phi = -1$ represent the first (gas) and second (liquid) fluid, respectively. The iso-surface of $\phi(\mathbf{x}, t) = 0$ marks the free interface between gas and liquid at time t. In equation (3), $h(\phi) = \frac{1}{\eta^2}\phi(\phi^2 - 1)$ is from the assumption of double-well potential, where η is the interface thickness parameter. Also $\lambda = \frac{3}{2\sqrt{2}}\sigma\eta$ is the mixing energy density, where σ is the interfacial surface tension coefficient that is assumed to be constant throughout this paper, and γ_1 is the interface mobility. The value of γ_1 could substantially affect the simulation results and will be discussed in section 4. In particular, $\nu_E(\mathbf{x}, t) \geq 0$ is the so called entropy-viscosity that could stabilize the simulation of flow at high Reynolds number on a under-resolved mesh, while $C_\phi(\mathbf{x}, t)$ is a combined coefficient of diffusion and anti-diffusion, the definition of which will be clear in section 2.3. Diffusion ensures that the solution overshoot ($\phi > 1.0$) or undershoot ($\phi < -1.0$) are in a reasonable range, while anti-diffusion can sharpen the interface dynamically and adaptively. The density ρ and dynamic viscosity μ are defined by the following formulas,

$$\rho(\phi) = \frac{\rho_1 + \rho_2}{2} + \frac{\rho_1 - \rho_2}{2}\phi, \quad \mu(\phi) = \frac{\mu_1 + \mu_2}{2} + \frac{\mu_1 - \mu_2}{2}\phi, \tag{4}$$

where (ρ_1, μ_1) and (ρ_2, μ_2) are the pair of densities, dynamic viscosity of the first fluid (gas) and second fluid (liquid), respectively.

2.2. Entropy-viscosity method stabilization

In equation (1), the role that the scalar ν_E plays is similar to that of the eddy viscosity of LES models. Here, to simplify the calculation we will lump the value of the entropy-viscosity into a single number computed over an entire spectral element. The original formula of EVM was proposed by [15,24] and modified in [17,18] to compute the entropy-viscosity in each element K at the collocation points ijm as follows:

$$\nu_E|_K = \min\{\beta_E \|\mathbf{u}\|_{L^\infty(K)}\delta_K, \alpha_E \frac{\|R_{ijm}^K(\mathbf{u})\|_{L^\infty(K)}}{\|E_{ijm}^K(\mathbf{u}) - \bar{E}(\mathbf{u})\|_{L^\infty(\Omega_J)}}\delta_K^2\}, \tag{5}$$

where δ_K is the minimum distance between two quadrature points in element K, α_E and β_E are two model parameters. In this paper, unless explicitly stated otherwise, $\beta_E = 0.5$ is always used, while the value of α_E will be discussed in subsequent sections. Note that we use the maximum norm $L^\infty(K)$ over an element K, while $L^\infty(\Omega_J)$ over the region Ω_J, where $J = 1, 2$, represents the computational domain of $\phi \geq 0$ and $\phi < 0$, respectively. Here we note that the entropy-viscosity model is a promising new approach for LES, as the systematic simulations [17] of single phase turbulent pipe flow show that the eddy-viscosity of this model scales with the cube of the distance from the wall and approaches zero at the wall, which is theoretically correct. We define the various quantities as follows:

$$E_{ijm}^K(\mathbf{u}) = \frac{1}{2}(\mathbf{u}_{ijm}^K - \bar{\mathbf{u}}(\Omega_J))^2, \quad \bar{E}(\mathbf{u}) = \frac{\int_{\Omega_J} E_{ijm}^K(\mathbf{u}) \cdot d\mathbf{x}}{\int_{\Omega_J} d\mathbf{x}} \tag{6}$$

$$R_{ijm}^K(\mathbf{u}) = \mathbf{u} \cdot (\frac{\partial\mathbf{u}}{\partial t} + \mathbf{u} \cdot \nabla\mathbf{u} + \frac{\nabla p}{\rho} - \frac{\mu}{\rho}\nabla^2\mathbf{u} - \frac{\nabla\mu}{\rho} \cdot (\nabla\mathbf{u} + \nabla\mathbf{u}^{\mathbf{T}}) + \frac{\lambda}{\rho}(\nabla^2\phi)\nabla\phi - \frac{\mathbf{f}(\mathbf{x}, t)}{\rho})|_{ijm}^K, \tag{7}$$

where $\bar{\mathbf{u}}(\Omega_J)$ is the mean value of $\mathbf{u}$ in region Ω_J.

2.3. Entropy-viscosity method interface sharpening

A special difficulty for solving the fourth-order Cahn-Hilliard equation is that this equation cannot be discretized by C^0 spectral-element or finite-element method directly. To this end, [13] proposed the following second-order stabilization term added on the right hand side of equation (3),

$$S\frac{\lambda\gamma_1}{\eta^2}\nabla^2(\phi^{n+1} - \phi^{*,n+1}), \tag{8}$$

where S is a chosen constant satisfying $S \geq \eta^2\sqrt{\frac{4\gamma_0}{\lambda\gamma_1\Delta t}}$ and $\phi^{*,n+1} = \sum_{k=0}^{J_e}\beta_k\chi^{n-k}$ is the J_eth order extrapolation of ϕ^{n+1}, n is the time step number, Δt is the time step, and $\gamma_0 = \sum_k^{J_e}\alpha_k$, α_k and β_k are the weights of the stiffly-stable integration scheme, the values of which can be found in [25]. In the simulation of slug flow (see section 4), $\lambda\gamma_1 \propto \eta^2$, which gives rise to following estimation,

$$S\frac{\lambda\gamma_1}{\eta^2} \geq \eta\Delta t^{-0.5}. \tag{9}$$

The above equation indicates that although $\phi^{*,n+1}$ is a second-order approximation of ϕ^{n+1} with respect to Δt, the numerical diffusion introduced by the term in equation (8) is no longer negligible when η is large, which is very likely for the case of large scale simulation, and the results become worse when a long time simulation is involved. Therefore, in addition to its intrinsic diffusion, the method proposed in [13] introduces extra numerical diffusion. On one hand, numerical diffusion can smooth the solution making the simulation more stable, but on the other hand, one of the side effect due to the diffusion is that the interface is eventually thickened. Moreover, our experience of the simulation of the two-phase flow using realistic parameters shows that the diffusion introduced by the term in equation (8) is not an effective remedy in terms of stabilization.

To stabilize the simulation and limit the thickening effect simultaneously, a term that combines the entropy-viscosity and artificial interface compression is introduced to equation (3). We note that the idea of compressing the interface is not totally new, it is also used in the VoF method in OpenFoam [3,26,4]. Sometimes it is referred to as the anti-diffusion method, e.g., VoF method in [27], conservative level-set method in [9,28], while its original form was proposed by [29]. In our implementation, C_ϕ is defined as follows,

$$C_\phi = \left(1 - \frac{C_{\text{comp}}}{\nu_C}\frac{\|\mathbf{u}\|(1-\phi^2)}{\|\nabla\phi\|}\right)\nu_T, \tag{10}$$

where $\|\cdot\|$ is the Euclidean norm, and the term $1-\phi^2$ ensures that $\frac{C_{\text{comp}}}{\nu_C}\frac{\|\mathbf{u}\|(1-\phi^2)}{\|\nabla\phi\|}$ is non-negative and only active in the interfacial area where $-1 < \phi < 1$. ν_T is the entropy-viscosity for the Cahn-Hilliard equation, the definition of which will become clear shortly; ν_C is the normalization of ν_T, the value of which can be obtained by using following formula,

$$\nu_C = \frac{\lambda\gamma_1}{\eta^2}. \tag{11}$$

Note that the level of compression depends on the adjustable constant C_{comp}. In this paper, unless explicitly mentioned otherwise, we take $C_{\text{comp}} = 0.1$. The value of ν_T is obtained by the following equations,

$$\nu_T|_K = \min\{\beta_T\|\mathbf{u}\|_{L^\infty(K)}\delta_K, \alpha_T\frac{\|R^K_{ijm}(\phi)\|_{L^\infty(K)}}{\|E^K_{ijm}(\phi) - \bar{E}(\phi)\|_{L^\infty(\Omega)}}\delta_K^2\}, \tag{12}$$

where α_T and β_T are two parameters. Again, in this paper, unless explicitly mentioned otherwise $\beta_T = 0.5$, thus only α_T is the free parameter. In the above equations, the various quantities are defined as follows:

$$E^K_{ijm}(\phi) = \frac{1}{2}(\phi^K_{ijm} - \overline{\phi}(\Omega))^2, \quad \bar{E}(\phi) = \frac{\int_\Omega E^K_{ijm}(\phi)\cdot d\mathbf{x}}{\int_\Omega d\mathbf{x}} \tag{13}$$

$$R^K_{ijm}(\phi) = \phi\cdot(\frac{\partial\phi}{\partial t} + \mathbf{u}\cdot\nabla\phi + \lambda\gamma_1\nabla^2\left[\nabla^2\phi + h(\phi)\right])|^K_{ijm}. \tag{14}$$

We note the difference between Ω_J used in equations (5)-(7) and equations (12)-(14). We also note that if $\nu_C = \|\mathbf{u}\|h_{\text{reg}}$, the current artificial interface compression model by equation (10) is equivalent to the anti-diffusion model proposed in [9, 28], where h_{reg} is a regularized version of mesh size. An alternative method was proposed by [12] who employed variable fractional order derivatives to control the sharpness of the interface in their phase-field simulation.

The above coupled system of equations is solved by the algorithm proposed in section 2.2 of [13], which was subsequently extended to the simulation of N-phase flow [30,31], heat transfer of two-phase flow [32] and pipe vibration induced by internal two phase flow [33], which are all at low Reynolds number. The algorithm uses a velocity-correction scheme to update the velocity field and pressure field in the Navier-Stokes equations with variable density and viscosity. In space, equal-order spectral-element discretization is used for the velocity and the pressure over a $(x-y)$ plane, and Fourier expansion is used in the homogeneous direction (z direction) [34,25]. The advantage of the algorithm is that only constant (time-independent) coefficient matrices are involved after discretization, despite the fact that the coupled system is associated with the variable density and variable viscosity. Another attractive feature of this algorithm is its capability of dealing with large density ratios. However, as we mentioned before, for simulation of two-phase flows using realistic parameters, the challenges come from both the large density ratio *and* the high Reynolds number, hence the entropy-viscosity approach is necessary to ensure the simulation remains stable.

3. Verification and convergences rates

In the aforementioned method, there are two free parameters, namely α_E for EVM in Navier-Stokes equations and α_T in the Cahn-Hilliard equation. In this section, we will study the sensitivity due to these two parameters. For all the simulations in this section, we use dimensionless parameters.
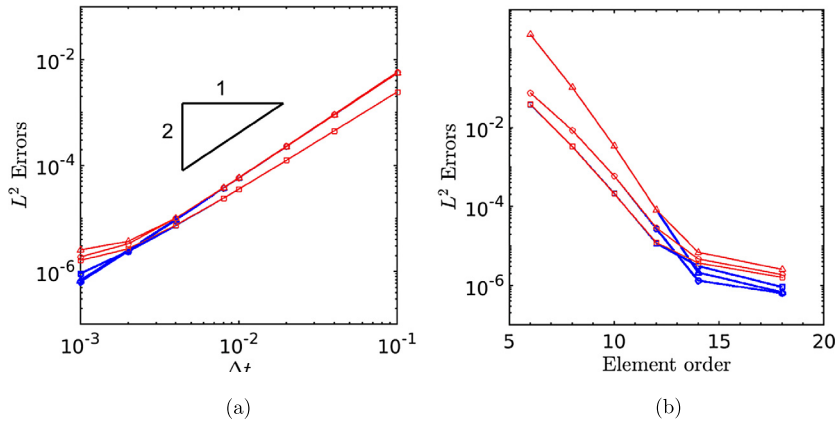
Fig. 1. Temporal (a) and spatial (b) convergence rates of L^2 errors against the fabricated smoothed solution: line with circles, velocity (x component u); line with triangles, pressure p; line with squares, phase-field variable ϕ. Blue lines represent the DNS ($\alpha_E = 0.0$ and $\alpha_T = 0.0$) results and red lines represent the results of simulation using both EVM stabilization and AICM with $\alpha_E = 10^{-3}$, $\alpha_T = 10^{-3}$. (For interpretation of the colors in the figure(s), the reader is referred to the web version of this article.)

3.1. Convergence rates for analytic solution

Here we test the accuracy of the method for the coupled system of Navier-Stokes equations and Cahn-Hilliard equation by employing a manufactured solution that was also used by [13,32]. We consider a cubic domain $\Omega = (x, y, z): 0 \le x \le 2, -1 \le y \le 1, 0 \le z \le 2$ and the analytic solution is defined as follows,

$$u(x, y, z) = A \cos(a_0 x) \cos(b_0 y) \cos(c_0 z) \sin(w_0 t),$$
$$v(x, y, z) = 0,$$
$$w(x, y, z) = B \sin(a_0 x) \cos(b_0 y) \sin(c_0 z) \sin(w_0 t), \tag{15}$$
$$\phi(x, y, z) = A_1 \cos(a_1 x) \cos(b_1 y) \cos(c_1 z) \sin(w_1 t),$$

where $A = 1.0$, $a_0 = \pi$, $b_0 = \frac{3}{2}\pi$, $c_0 = 1.0$, $w_0 = 1.0$, $A_1 = 1.0$, $a_1 = \pi$, $b_1 = \pi$, $c_1 = \pi$ and $w_1 = 1.0$. Note that during the simulation, a time-dependent body force for the Navier-Stokes equation and a source to the Cahn-Hilliard equations is imposed, which can be obtained by substituting the solution of (15) to the corresponding equations. On the four boundaries of the rectangular domain $[0, 2] \times [-1, 1]$ that was partitioned into two quadrilateral elements along the x direction evenly, Dirichlet boundary conditions for the velocity are imposed, while a homogeneous Neumann boundary condition is employed for the Chan-Hilliard equation. The initial condition is obtained from the solution of equation (15) by setting $t = 0$, and we use following set of parameters,

$$\rho_1 = 1.0, \quad \rho_2 = 3.0, \quad \mu_1 = 0.01, \quad \mu_2 = 0.02,$$
$$\lambda = 10^{-3}, \quad \gamma_1 = 10^{-3}, \quad \eta = 10^{-2}. \tag{16}$$

To obtain the convergence rate with respect to time step Δt, we have fixed the spectral element order to be 18 and systematically varied the Δt. For each Δt, we perform the simulation from $t = 0$ to $t = 1$, then compute the L^2 errors of the velocity, pressure and phase-field variable at $t = 1.0$. In space, in order to achieve spectral convergence, we have fixed the $\Delta t = 10^{-3}$ and systematically increased the spectral element order from 6 to 18, and the L^2 errors are calculated at $t = 1.0$. We note that both EVM and AICM with $\alpha_E = 10^{-3}, \alpha_T = 10^{-3}$, are employed for solving the Navier-Stokes equations and the Cahn-Hilliard equation. Fig. 1a plots the temporal error variation with Δt. We see that the method can achieve a second-order convergence rate for velocity and pressure, when the values of the parameters α_E and α_T are as small as 10^{-3}. The convergence rate of phase-field variable is second-order at large Δt, but it reduces to approximate 1.9, when $\Delta t \le 2 \times 10^{-2}$. Fig. 1b demonstrates the exponential convergence with respect to the spectral element order. As shown in this plot, the method with EVM and AICM is as accurate as that of DNS when the element order is up to 12 and produces slightly larger errors when the spectral element order is beyond 12.

3.2. The three-dimensional LeVeque benchmark test

In this section, we perform three-dimensional tests for the problem proposed by [35], which is often used in testing the level-set [36,9] and VoF [37] methods. However, to the best of our knowledge, this problem has not been tested using the

(a) $N_z = 64$
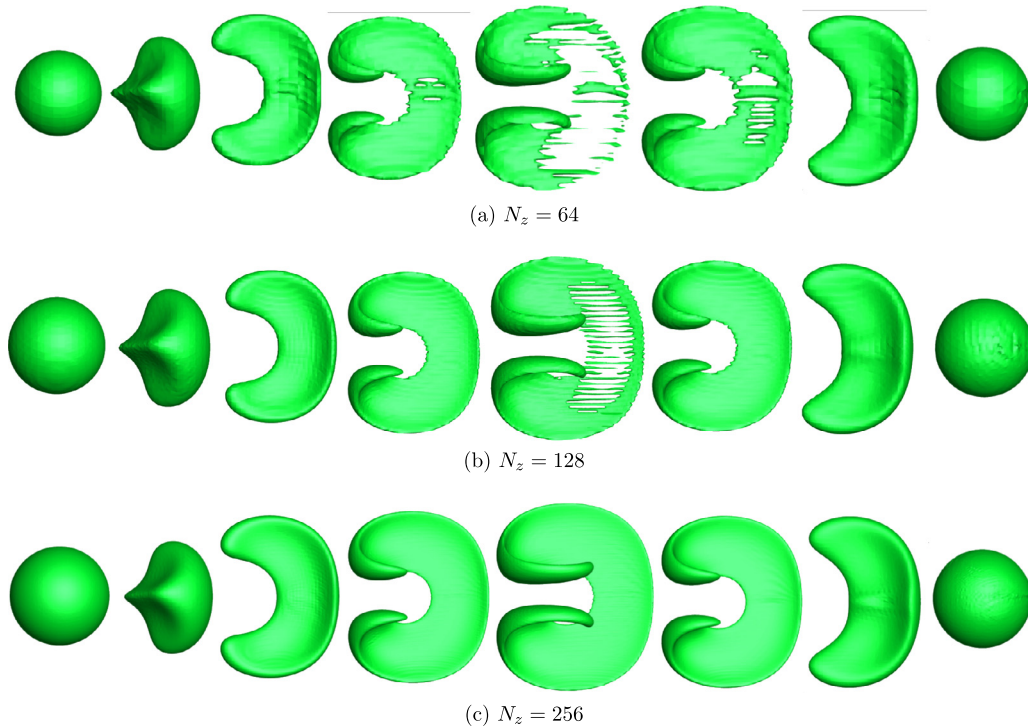
(b) $N_z = 128$

(c) $N_z = 256$

Fig. 2. Phase-Field simulation result of the interface evolution of the three dimensional LeVeque problem for different resolutions, (a) $N_z = 64$, (b) $N_z = 128$, (c) $N_z = 256$. Snapshots are at time $t = 0$, 0.3, 0.6, 1.0, 1.5, 2.0, 2.5, 3.0, from the left to right. Here, we have set $\lambda\gamma_1 = 10^{-11}$ and $\alpha_T = 0.1$.

phase-field method before. For this problem, the velocity vector $\mathbf{u} = (u, v, w)$ in the unit cubic computational domain is given by

$$
\begin{aligned}
u(x, y, z) &= 2\sin^2(\pi x)\sin(2\pi y)\sin(2\pi z)\cos(\pi t/T), \\
v(x, y, z) &= -\sin(2\pi x)\sin^2(\pi y)\sin(2\pi z)\cos(\pi t/T), \\
w(x, y, z) &= -\sin(2\pi x)\sin(2\pi y)\sin^2(\pi z)\cos(\pi t/T),
\end{aligned}
\tag{17}
$$

where $T = 3$ is the time period. The initial field of ϕ is given by

$$
\phi(x, y, z) = -\tanh\left(\frac{\sqrt{(x - x_0)^2 + (y - y_0)^2 + (z - z_0)^2} - R}{\sqrt{2}\eta}\right),
\tag{18}
$$

where $x_0 = y_0 = z_0 = 0.35$, $R = 0.15$. As shown in equation (18), initially, the interface forms a sphere, and subsequently it is stretched out by the velocity field shown in equation (17). In particular, it develops a very thin film at $t = T/2$, which could be under-resolved depending on the mesh resolution and volume loss due to numerical diffusion. The interface recovers the sphere at $t = T$.

Here the solutions were obtained from three different grids: on *grid 1*, the unit square in the $x - y$ plane is partitioned into 13×13 quadrangles and 64 Fourier planes along z direction; on *grid 2*, the domain is partitioned into 26×26 quadrilateral elements and 128 Fourier planes; on *grid 3*, the domain consists of 42×42 quadrilateral elements and 256 Fourier planes. In all three simulations, we have used 5 spectral-element modes and a constant time step $\Delta t = 6.25 \times 10^{-4}$.

For the LeVeque problem, the evolution of the interface is governed by an advection equation, which is different form the Cahn-Hilliard equation (3), where on the right-hand-side there is a diffusion term that is controlled by the coefficient $\lambda\gamma_1$. In the test, we have used $\lambda\gamma_1 = 10^{-11}$ to minimize the effect of the diffusion. For all the simulations in this section, $\alpha_T = 0.1$ is used to obtain ν_T.

Fig. 2 shows the time series of the iso-surfaces of $\phi = 0$ for different resolutions. We see that for the case using 64 Fourier planes, the phase-field simulation can almost recover the sphere after one period, which is significantly better than the corresponding result presented in [36]. Using 128 Fourier planes, our simulation result is as good as that presented in [9] on a mesh with resolution 100^3. Increasing the number of Fourier planes to 256, the current phase-field simulation can achieve very smooth iso-surface and recover the sphere after one period almost perfectly, which is comparable with the VoF simulation published in [37] using a mesh resolution of 200^3, as well as the level-set simulation in [38] on a mesh consisting of 512^3 cells.
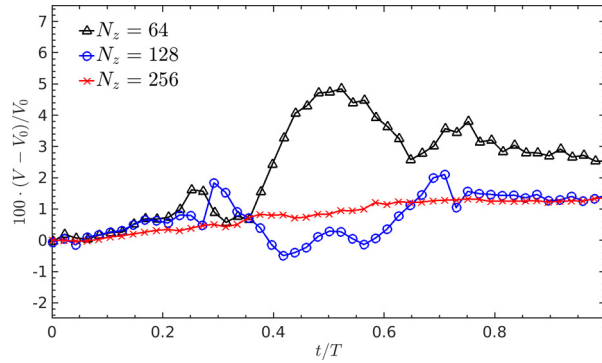
Fig. 3. Volume loss of the second fluid ($\phi \leq 0$) from the phase-field simulation of the three-dimensional LeVeque problem at different resolutions. Black line $N_z = 64$, blue line $N_z = 128$, red line $N_z = 256$.

Fig. 3 shows the volume loss from the phase-field simulation for different resolutions. We observe that in the worst scenario the volume loss error rises up to near 5%, for the mesh consisting of 64 Fourier planes, around time $t = \frac{T}{2}$, when the iso-surface develops a very thin film. However, when the resolution is increased to 128 and beyond, the volume loss error is less than 2% for the whole simulation duration.

3.3. Two-dimensional air bubble rising in a water container

In this section, in order to further evaluate the performance of EVM and AICM, following the work in [13], we have performed simulations of a two-dimensional air bubble rising in a closed water container. Specifically, we have considered the case that the container's size is 2 cm × 3 cm and a bubble diameter is 1 cm. Note that here we still use non-dimensional parameters, and the normalization is the same as that in section 3.3 of [13]. The computational domain is a rectangle: $\Omega = \{(x, y) : -0.5 \leq x \leq 0.5, 0.0 \leq y \leq 1.5\}$ that consists of 28×42 quadrilateral elements. Initially, the water is still and a circular air bubble with radius $R_0 = 0.25$ is placed at $(x_0, y_0) = (0, 0.5)$, which corresponds to the following initial condition for the Cahn-Hilliard equation,

$$\phi(x, y) = -\tanh\left(\frac{\sqrt{(x - x_0)^2 + (y - y_0)^2} - R_0}{\sqrt{2}\eta}\right). \tag{19}$$

We have used the following physical parameters,

$$\begin{aligned}
\rho_1 &= 1.0, & \rho_2 &= 829.08, \\
\mu_1 &= 5.2 \times 10^{-3}, & \mu_2 &= 0.2927, \\
\sigma &= 151.1628, & g &= -9.8,
\end{aligned} \tag{20}$$

as well as following numerical parameters,

$$\eta = 0.01, \quad \lambda \gamma_0 = 10^{-7}, \tag{21}$$

where g is the non-dimensional gravitational acceleration along the $-y$ direction. In all the simulations, 5 spectral-element modes and a time step $\Delta t = 2.5 \times 10^{-3}$ are used.

Fig. 4 shows snapshots of the bubble interface at different value of α_T, before it reaches the top wall. The difference is negligible among the results from the simulations using $\alpha_T \leq 0.01$, while for the simulation using $\alpha_T = 0.1$, the result is slightly different at the position where the interface has large curvature, see the figure of $t = 1.275$. In Fig. 5 we plot the time history of the lost liquid volume for the four cases. Similarly as previously, we see that the volume losses for the simulations using $\alpha_T \leq 0.01$ are indistinguishable, while the loss for $\alpha_T = 0.1$ is slightly larger than the previous simulations, but the overall loss is within 2% when the simulation reaches $t = 2.5$.

To summarize, our phase-field method based on the SEF can achieve second-order temporal accuracy and spectral spatial convergence for fabricated smooth solutions, which results in better simulation results compared with the Level-Set or VoF method using the low-order finite element or finite volume discretization. From the simulation of the rising air bubble in a water container, we find that the solution of the Cahn-Hilliard equation is not very sensitive to the entropy-viscosity, when the parameter $\alpha_T \leq 0.1$.
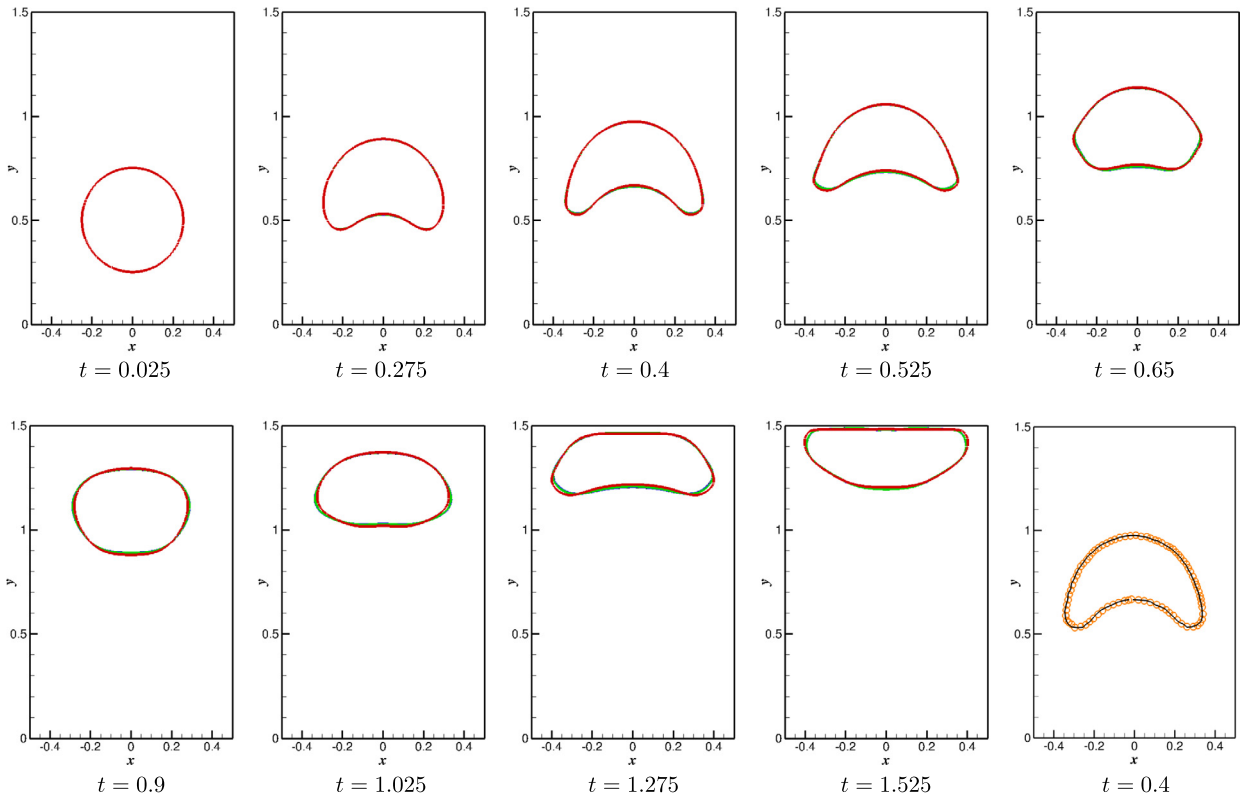
Fig. 4. Time sequence of snapshots of a rising air bubble in a water container. Black line, DNS ($\alpha_E = 0$, $\alpha_T = 0$); blue line, $\alpha_E = 0.01$, $\alpha_T = 0$; green line, $\alpha_E = 0.01$, $\alpha_T = 0.01$; red line, $\alpha_E = 0.01$, $\alpha_T = 0.1$. Initially, the air bubble is a circle of diameter 1 cm, the size of the container is 2 cm × 3 cm. The last lower right plot shows a direct comparison between current DNS result and previous results of [13] (orange circles) at $t = 0.4$.
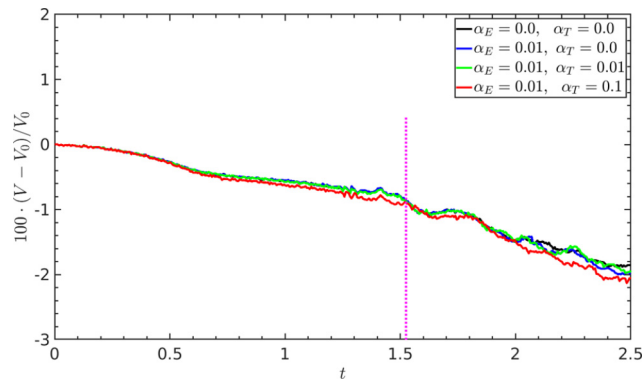

Fig. 5. Time history of the lost liquid volume for the simulation of a rising air bubble in a water container. V_0 is the initial volume of liquid, V is the instantaneous value from the simulations. The vertical dashed line corresponds to $t = 1.525$, when the bubble reaches the top wall.

4. Application to slug flow

In this section, we will apply our method to simulate the two-phase slug flow initiating from the stratified flow in a horizontal pipe of diameter $D = 54$ mm. Note that this diameter is often used in experiments and simulations, see [39, 26,40]. A pipe aspect ratio $\frac{L_z}{D} \geq 150$ with inflow and outflow boundary conditions is often used both in experiments [41, 42] and simulations [43], but the study of [39] found that it is difficult to exclude the artificial boundary effects in the simulation if inlet and outlet boundary conditions are used, while the effect is less pronounced for periodic boundary conditions. Nonetheless, the successful simulation [39] of slug flow with periodic boundary conditions in a shorter pipe ($\frac{L_z}{D} = 74.1$) clearly shows the advantages of using periodic boundary condition in simulations of slug flows in a very long pipe. Here we have carried out our simulations in a pipe with a length $L_z = 75D$. Different from previous sections, here we
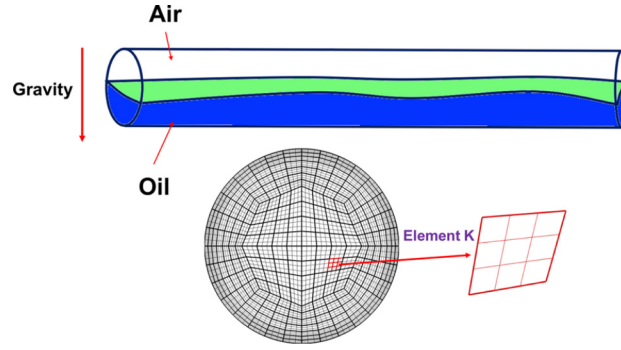
Fig. 6. A sketch of the two-phase oil/air flow in a horizontal pipe of diameter D and the spectral element mesh for a cross section. In the pipe, the blue color area is oil, blank area is air and green color indicates the interfacial area. On the cross-section ($x - y$ plane), there are 288 quadrilateral prismatic elements, while along the pipe axis direction (z direction), Fourier expansion is used. Note that for the elements on the cross-section, the maximum edge length is $0.0716D$ and the minimum length is $0.0165D$.

have used dimensional parameters. The physical properties of the two fluids have realistic values corresponding to air and Shell Tellus 22 oil measured by [41], and are listed below,

$$
\begin{aligned}
\rho_1 &= 1.18 \text{ kg/m}^3, & \rho_2 &= 860 \text{ kg/m}^3, \\
\mu_1 &= 1.83 \times 10^{-5} \text{ kg/(m} \cdot \text{s)}, & \mu_2 &= 6.0 \times 10^{-2} \text{ kg/(m} \cdot \text{s)}, \\
\sigma &= 3.0 \times 10^{-2} \text{ kg/s}^2, & g &= -9.8 \text{ m/s}^2.
\end{aligned}
\tag{22}
$$

Note that the above parameters result in a density ratio and viscosity ratio:

$$
\frac{\rho_2}{\rho_1} = 728.81, \quad \frac{\mu_2}{\mu_1} = 3\,287.7.
\tag{23}
$$

The computational domain consists of 288 quadrilateral elements, as shown in the bottom panel of Fig. 6. On the pipe wall we have imposed homogeneous Dirichlet boundary conditions for velocity and homogeneous Neumann boundary conditions for the Cahn-Hilliard equation. We assume the initial oil/air two phase flow system is fully segregated, with air flowing above the oil and parallel to the pipe axis, as sketched in the top panel of Fig. 6, while the initial height of oil level along the pipe is given by [39] as follows,

$$
\phi(x, y, z) = \tanh\left(\frac{y + 0.2R \sin(4\pi \frac{z}{L_z})}{\sqrt{2}\eta}\right),
\tag{24}
$$

where $R = 27$ mm is the radius of the pipe. Note that the above formula results in the air and oil volume fraction of 50% and a sinusoidal disturbed free surface. In equation (24), the interface thickness parameter η is determined by the resolution of the simulations. In previous work, [44] reported that their phase-field method implemented in a Fourier code requires $7 - 10$ grid points across the interface to avoid numerical instabilities. Here, our own experience shows that the following rule is adequate to eliminate the spurious errors,

$$
\eta = 1.2 \frac{L_z}{N_z},
\tag{25}
$$

where N_z is the number of Fourier planes along the pipe. Note that for the current simulations, the above equation automatically fulfills the resolution requirement on the cross section, where 3 spectral element modes are used, which results in a finer mesh grid point on the $x - y$ plane than that on z direction. In the rest of this section, we will present simulation results for the following two cases:

$$
case\ 1,\ N_z = 1024; \quad case\ 2,\ N_z = 2048.
$$

Moreover, the initial velocity field is obtained from our previous simulation of single phase flow [17], which is a fully developed turbulent flow at $Re_D = 5\,300$. To be precise, the initial bulk velocity re-scaled to $U_{bulk} = 0.1$ m/s.

In both simulations, we have employed a constant time step $\Delta t = 10^{-5}$ s, and entropy-viscosity parameter $\alpha_E = 0.1$, $\alpha_T = 0.1$. A dynamic driving force is used to maintain the air superficial velocity $U_{sg} = 2$ m/s as follows,

$$
F_z = \rho_1 \frac{U_{inst} - U_{sg}}{\Delta t},
\tag{26}
$$

where F_z is z-component of the driving force and U_{inst} is the instantaneous air superficial velocity calculated at each time step. In the simulation, the above driving force accelerates the air superficial velocity to the target $U_{sg} = 2$ m/s after 250 iterations, while the oil superficial velocity U_{sl} keeps increasing during the entire simulation reaching the value 1.68 m/s after 125 000 iterations. It is worth noting that the pair of superficial velocities $\{U_{sg}, U_{sl}\}$ is located inside the well-defined slug flow regime, see the flow pattern map in [45]. Also note that the characteristic Reynolds numbers for the current simulation are as follows,

$$Re_{sg} = \frac{\rho_1 U_{sg} D}{\mu_1} = 6\,964, \;\; Re_{sl} = \frac{\rho_2 U_{sl} D}{\mu_2} \approx 1\,300, \tag{27}$$

where $U_{sl} \approx 1.68$ m/s is obtained at $t = 1.25$ s.

Before advancing to the simulation results, there is one more parameter to determine, that is the interface mobility γ_1. In the previous section of the simulation of a rising air bubble in a water container, we have used the rule of [13] to determine the value of interface mobility γ_1, which reports that the simulation results are virtually the same when $\gamma_1^* \leq 10^{-4}$, where $\gamma_1^* = \frac{3\sigma\gamma_1}{2\sqrt{2}D^2 U_{sg}}$ is the mobility number [46]. However, in the literature, γ_1^* is usually assumed to be a function of $Cn = \frac{\eta}{D}$, e.g., the following scaling law was suggested by [47,46,48],

$$\gamma_1^* = M_0 \, Cn^M, \tag{28}$$

where M_0 and M are model constants. Actually, [47] proposes that $1 < M \leq 2$, concerning the relationship among diffusion, strain and chemical potential, while [46] gives a theoretical scaling law to calculate the optimal value, i.e. $\gamma_1^* = 3Cn^2$. More recently, in a series of papers [48,49] rigorously proved that the phase-field model converges to sharp interface method when $M = 0$ or $M = 1$, but this is not true when $M > 3$. Based on the above studies, we have used the following scaling law in our simulation of slug flows,

$$\gamma_1^* = 0.2 \, Cn. \tag{29}$$

We find that the above relationship leads to successful simulations of slug flow initiated from stratified flow, both for *case* 1 with $Cn = 0.0879$ and *case* 2 with $Cn = 0.0439$.

Fig. 7 exhibits the whole process of slug initiation and propagation along the pipe. Initially, at $t = 0.005$ s, the interface is smoothed but it is quickly transformed into a wavy structure at $t = 0.13$ s. The wave height keeps rising, and by $t = 0.23$ s, there are two notable large wave structures, one is in the middle and the other one is close to the right end of the pipe. At $t = 0.29$ s, as the large wave exits the right end and enters from the left end (note we use periodic boundary condition), it has gained more liquid and developed into a full slug, while the large wave on the middle also grows, but its size is not large enough to block the whole air flow passage. Note that for *case* 2, the full slug first forms at $t = 0.277$ s, while for *case* 1, the slug first forms at $t = 0.227$ s. Subsequently, the slug picks up more liquid as it is moved downstream by air flow and the large wave on the middle is still growing, see the snapshot at $t = 0.405$ s. Surprisingly, the slug becomes shorter and the height of the large wave is decreased when time reaches $t = 0.62$ s. The length of the slug grows continuously after $t = 0.77$ s, and notably, there is air entrained into the liquid slug body. Meanwhile, the previous large wave in the middle has totally disappeared, as shown in the snapshots at $t = 1.0$ s and $t = 1.20$ s. Fig. 8 shows the corresponding vortical flow structures in the pipe. At $t = 0.005$ s, small scale vortices are uniformly distributed in the gas flow, but the vortices quickly concentrate in an area where the wave is rising, as shown in the second snapshot from the top. By the time when the slug is fully formed, which is shown in the fourth snapshot, considerably more vortical structures are generated inside the pipe and there is a steep pressure drop between the slug front and the tail. As the slug is moving downstream and picking up more liquid, more vortical structures are produced in the area where free interface is evolving and changing rapidly.

Fig. 9 plots the liquid holdup along the pipe at time instant $t = 1.05$ s (black line) and $t = 1.075$ s (blue line). Here liquid holdup is defined as the ratio of the area occupied by liquid and the area of the entire cross-section. In Fig. 9, we compare the locations of the slug front at $t = 1.05$ s and $t = 1.075$ s. We can observe the fact that the slug moves a distance of $2.38D$, but the large wave shown on the left of the plot only moves a distance of $1.87D$ during the same time interval, indicating that the slug moves faster than a wave. The simulation result that the slug translational velocity U_F is larger than the averaged air flow speed $U_s = 2U_{sg}$ is consistent with the experimental observations in [50,51]. For this particular case, the relationship $U_F = 1.29U_s$ is in good agreement with the experimental correlation proposed in [51], which shows that U_F is in a range of $1.25 - 1.3 U_s$ for the situation that slug has notable aeration. This figure also shows that at $t = 1.075$ s, the length of the slug has increased to about $12D$. The slug length is still growing, and when $t = 1.20$ s, the length is over $17D$, which is consistent with the experimental measurements, see Table 1. Fig. 10 shows the evolution of the slug signals at different axial locations. The overall patterns of these signals are very similar to the experimental measurements presented in [52].

5. Concluding remarks

We have presented a stabilized phase-field method based on the entropy-viscosity method (EVM) for simulating two-phase flows at high Reynolds number, large density and viscosity ratios. We have introduced an artificial interface compres-
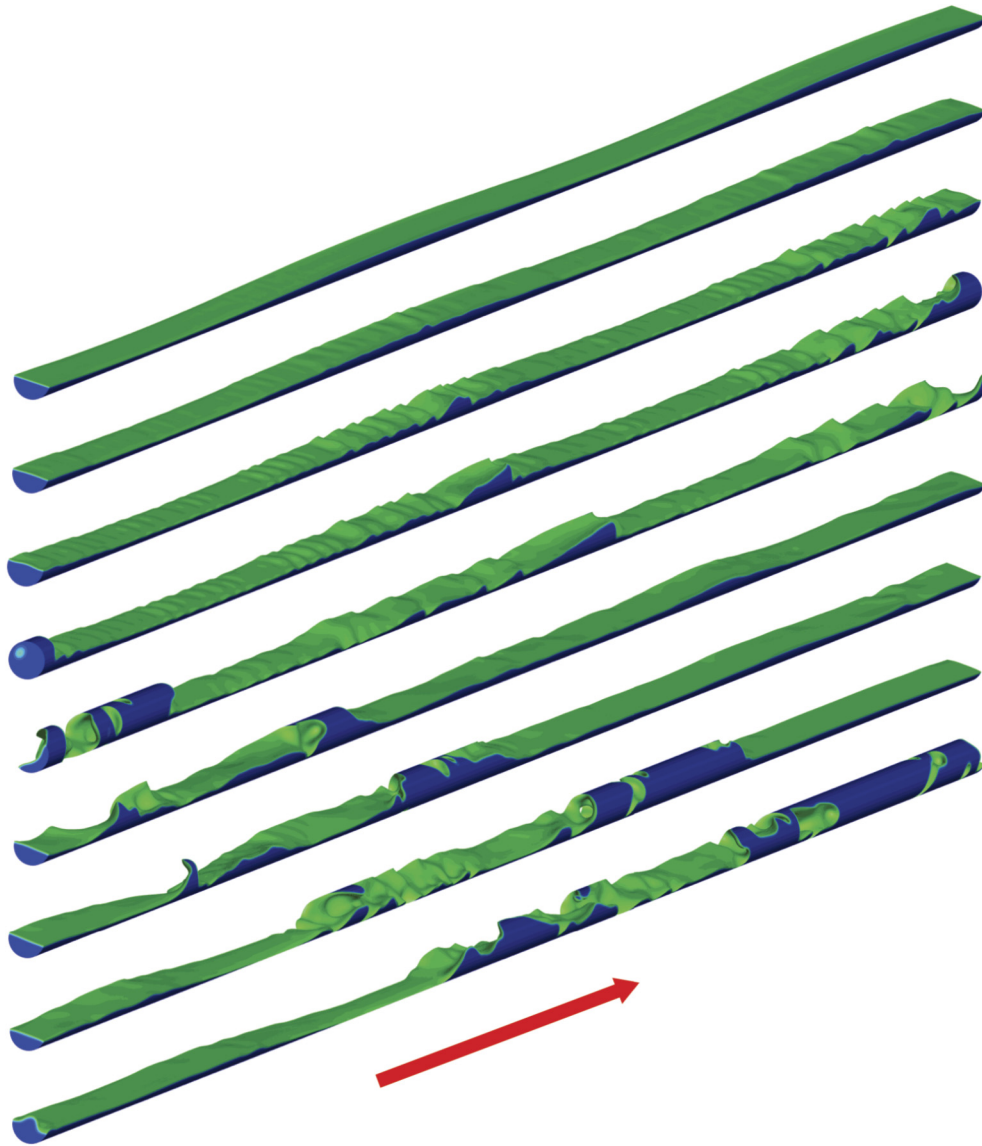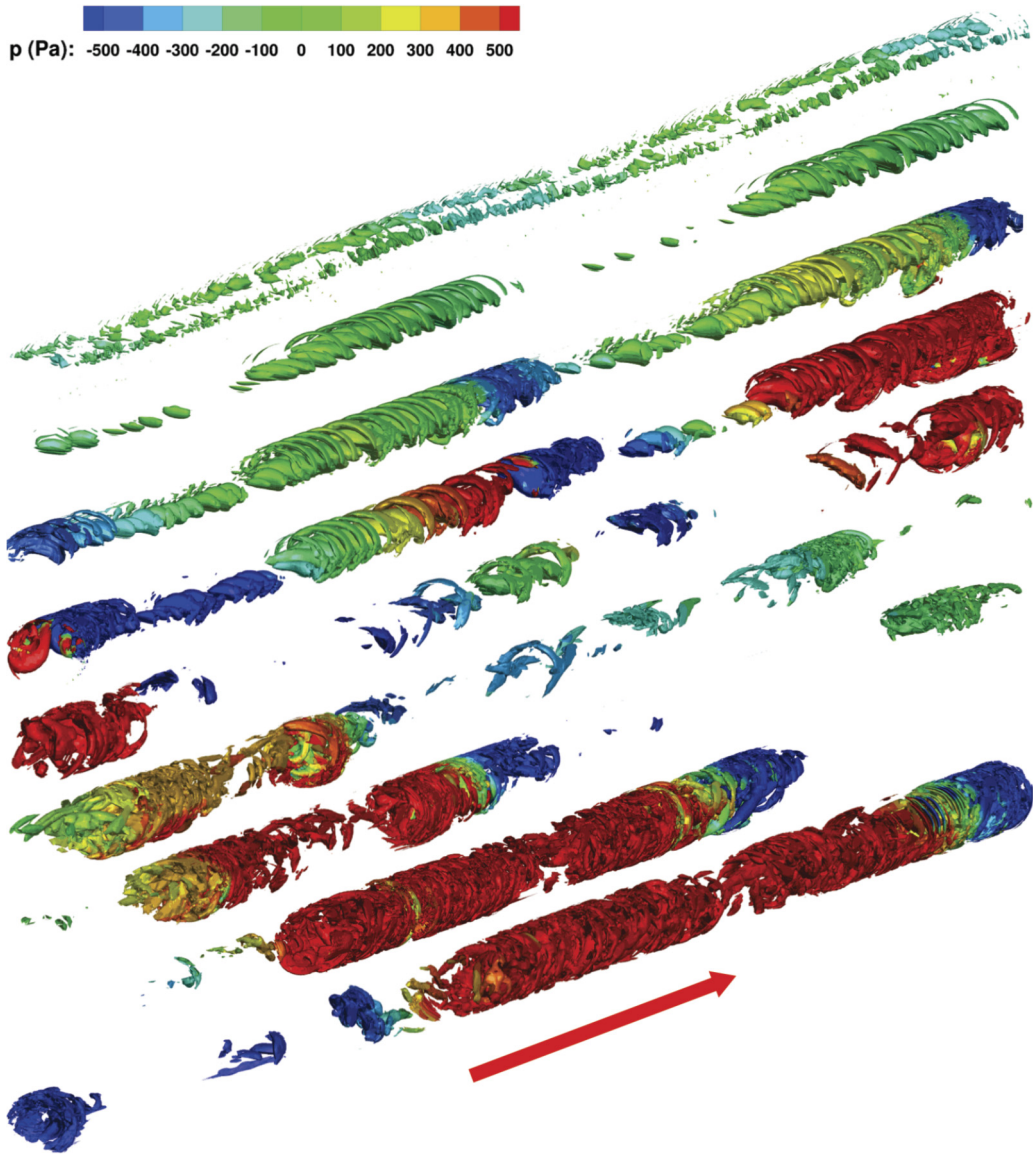
Fig. 7. Time sequence of snapshots of the slug initiation and propagation along the 4 m long horizontal pipe. Note that in each snapshot, the blue color area is occupied by oil, while the green area is the interface between oil and air. The volume fraction of the air is 50%. View from top to bottom: $t = 0.005$ s; $t = 0.13$ s; $t = 0.23$ s; $t = 0.29$ s; $t = 0.405$ s; $t = 0.62$ s; $t = 0.77$ s; $t = 1.00$ s; $t = 1.20$ s. Flow is from left to right.

Table 1
Predicted slug length using the SEF-EVM. Note that *case* 1 and *case* 2 have same resolution on the pipe cross-section, but the former uses 1024 Fourier planes, while the latter uses 2048 Fourier planes. For both cases, the slug length is obtained at $t = 1.25$ s. The definition of slug length is shown in Fig. 9. The VoF simulation of [53] and level-set simulation of [41] are done by commercial software TransAT and Fluent, respectively.

Study	Method	Fluids	D (mm)	$\frac{L_z}{D}$	$\frac{L_s}{D}$
case 1	phase-field	air-oil	54	75	**9.44**
case 2	phase-field	air-oil	54	75	**16.48**
[53]	VoF	air-water	20	200	15-20
[41]	level-set	air-water	78	205	2-4
[54]	experiment	air-water	53	321	15-20

sion technique that is also based on EVM for sharpening the interface. We have detailed the method that is implemented using Fourier/spectral-element discretization and gave explicit values for the parameter α_E and α_T. The method can achieve

Fig. 8. Time sequence of snapshots of the vortices in the 4 m long horizontal pipe. The vortices are represented by iso-surfaces of Q-criterion $Q = 1.5 \frac{U_{sg}^2}{D^2}$ and colored by the magnitude of pressure p. The time of each snapshot is same as the corresponding slug images in Fig. 7.

second-order accuracy in time and spectral convergence in space for smoothed fabricated solutions. The simulation tests confirm that the method is very accurate and the simulation results are not very sensitive to the values of α_E and α_T.

We have applied the method to simulate the initiation and evolution of air-oil slug in a horizontal pipe of diameter 54 mm and length 4 m using realistic physical parameters. The simulated slug body shows complex topology and air bubble entrainment. The liquid holdup signals from the simulation are very similar to those of the experiment. The predicted slug length and slug translational velocity are in excellent agreement with the experimental measurements. However, the small scale interfacial topology changes, such as small droplet injected into the air and small gas bubble entrained into liquid, which are observed in experiments, were not obtained in current simulations, due perhaps to the limitation of the resolution.

Acknowledgements
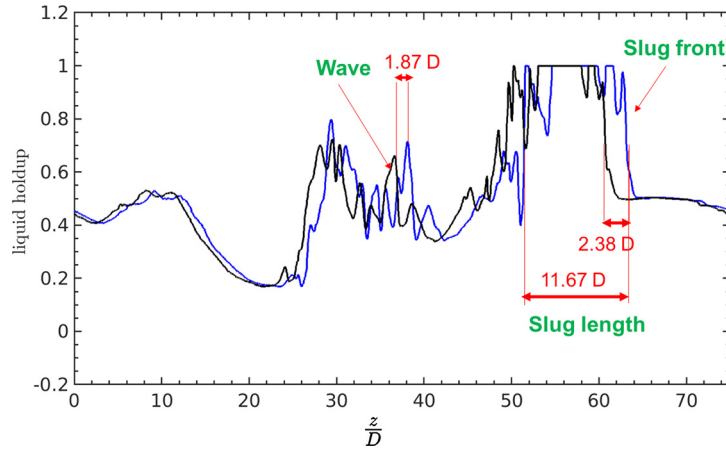
Fig. 9. Liquid holdup along the pipe at different time instants: black line, $t = 1.05$ s; blue line, $t = 1.075$ s. Flow is from the left to the right. Note that during the time interval $\Delta t = 0.025$ s, the slug translates $2.38D$, the large wave moves $1.87D$, while the displacement of air is $2U_{sg}\Delta t = 1.85D$. The slug translational velocity is 1.29 times that of air flow.
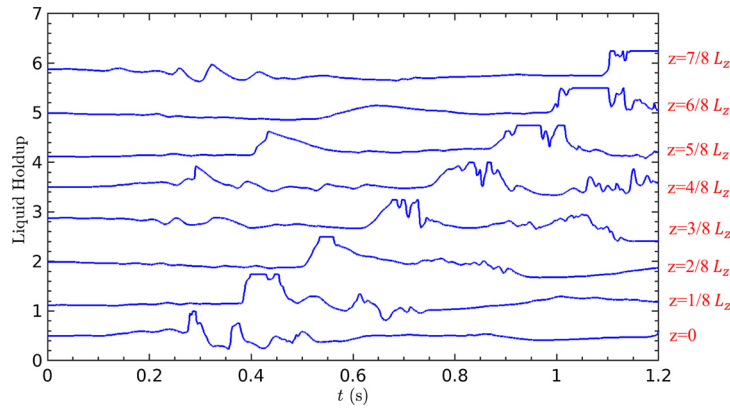
Fig. 10. Time series of liquid holdup signals illustrating the slug propagation along the pipe. L_z is the length of the pipe, $z = 0$ is at the left end of the pipe, and flow is from left to right.

References

[1] J. Pilliod, E.G. Puckett, Second-order accurate volume-of-fluid algorithms for tracking material interfaces, J. Comput. Phys. 199 (2003) 465–502.

[2] E. Aulisa, S. Manservisi, R. Scardovelli, S. Zaleski, Interface reconstruction with least-squares fit and split advection in three-dimensional Cartesian geometry, J. Comput. Phys. 225 (2007) 2301–2391.

[3] H.G. Weller, A New Approach to VOF-Based Interface Capturing Methods for Incompressible and Compressible Flow, Tech. Rep., OpenCFD Ltd., 2008.

[4] D.A. Hoang, V.V. Steijn, L.M. Portela, M.T. Kreutzer, C.R. Kleijn, Benchmark numerical simulations of segmented two-phase flows in microchannels using the volume of fluid method, Comput. Fluids 86 (2013) 28–36.

[5] S. Osher, R.P. Fedkiw, Level set methods: an overview and some recent results, J. Comput. Phys. 169 (2001) 463–502.

[6] J.A. Sethian, Evolution, implementation, and application of level set and fast marching methods for advancing fronts, J. Comput. Phys. 169 (2001) 503–555.

[7] S. Gross, A. Reusken, Numerical Methods for Two-Phase Incompressible Flows, first edn., Springer, 2011.

[8] O. Desjardins, V. Moureau, H. Pitsch, An accurate conservative level set/ghost fluid method for simulating turbulent atomization, J. Comput. Phys. 227 (2008) 8395–8416.

[9] J.-L. Guermond, M.Q. de Luna, T. Thompson, An conservative anti-diffusion technique for the level set method, J. Comput. Appl. Math. 321 (2017) 448–468.

[10] M. Sussman, E.G. Puckett, A coupled level set and volume-of-fluid method for computing 3D and axisymmetric incompressible two-phase flows, J. Comput. Phys. 162 (2000) 301–337.

[11] Y. Chen, J. Shen, Efficient, adaptive energy stable schemes for the incompressible Cahn–Hilliard Navier–Stokes phase-field models, J. Comput. Phys. 308 (2016) 40–56.

[12] F. Song, C. Xu, G.E. Karniadakis, A fractional phase-field model for two-phase flows with tunable sharpness: algorithms and simulations, Comput. Methods Appl. Mech. Eng. 305 (2016) 376–404.

[13] S. Dong, J. Shen, A time-stepping scheme involving constant coefficient matrices for phase-field simulations of two-phase incompressible flows with large density ratios, J. Comput. Phys. 231 (2012) 5788–5804.

[14] S. Mirjalili, S.S. Jain, M.S. Dodd, Interface-capturing methods for two-phase flows: an overview and recent developments, in: Center for Turbulence Research Annual Research Briefs, 2017, 2017, pp. 117–135.

[15] J.-L. Guermond, R. Pasquetti, B. Popov, Entropy viscosity method for nonlinear conservation law, J. Comput. Phys. 230 (11) (2011) 4248–4267.

[16] J.-L. Guermond, R. Pasquetti, B. Popov, From suitable weak solutions to entropy viscosity, J. Sci. Comput. 49 (1) (2011) 35–50.

[17] Z. Wang, M.S. Triantafyllou, Y. Constantinides, G.E. Karniadakis, An entropy-viscosity LES study of turbulent flow in a flexible pipe, J. Fluid Mech. 859 (2019) 691–730.
[18] Z. Wang, M.S. Triantafyllou, Y. Constantinides, G.E. Karniadakis, A spectral-element/Fourier smoothed profile method for large-eddy simulations of complex VIV problems, Comput. Fluids 170 (2018) 84–96.
[19] Y. Taitel, D. Barnea, Two-phase slug flow, Adv. Heat Transf. 20 (1990) 83–182.
[20] R.V. Hout, D. Barnea, L. Shemer, Evolution of statistical parameters of gas–liquid slug flow along vertical pipes, Int. J. Multiph. Flow 27 (2001) 1579–1602.
[21] S. McKee, M.F. Tomé, V.G. Ferreira, J.A. Cuminato, A. Castelo, F.S. Sousa, N. Mangiavacchi, The MAC method, Comput. Fluids 37 (2008) 907–930.
[22] G. Tryggvason, R. Scardovelli, S. Zaleski, Direct Numerical Simulations of Gas-Liquid Multiphase Flows, first edn., Cambridge University Press, 2011.
[23] M. Ishii, T. Hibiki, Thermo-Fluid Dynamics of Two-Phase Flow, second edn., Springer, 2011.
[24] J.-L. Guermond, A. Larios, T. Thompson, Validation of an entropy-viscosity model for large eddy simulation, in: J. Fröhlich, H. Kuerten, B.J. Geurts, V. Armenio (Eds.), Direct and Large-Eddy Simulation IX, in: ERCOFTAC Series, vol. 20, 2015, pp. 43–48.
[25] G.E. Karniadakis, S. Sherwin, Spectral/hp Element Methods for Computational Fluid Dynamics, 2nd edition, Oxford University Press, Oxford, UK, 2005.
[26] M. Czapp, M. Utschick, J. Rutzmoser, T. Sattelmayer, Investigations on slug flow in a horizontal pipe using stereoscopic particle image velocimetry and CFD simulation with volume of fluid method, in: 20th International Conference on Nuclear Engineering Collocated With the ASME Power Conference, vol. 3, Anaheim, California, USA, 2012.
[27] K.K. So, X.Y. Hu, N.A. Adams, Anti-diffusion method for interface steepening in two-phase incompressible flow, J. Comput. Phys. 230 (2011) 5155–5177.
[28] L. Cappanera, J.-L. Guermond, W. Herreman, C. Nore, Momentum-based approximation of incompressible multiphase fluid flows, Int. J. Numer. Methods Fluids 86 (2018) 541–563.
[29] A. Harten, The artificial compression method for computation of shocks and contact discontinuities: III. Self-adjusting hybrid schemes, Math. Comput. 32 (1978) 363–389.
[30] S. Dong, An efficient algorithm for incompressible N-phase flows, J. Comput. Phys. 276 (2014) 5788–5804.
[31] S. Dong, Multiphase flows of N immiscible incompressible fluids: a reduction-consistent and thermodynamically-consistent formulation and associated algorithm, J. Comput. Phys. 361 (2018) 1–49.
[32] X. Zheng, H. Babaee, S. Dong, C. Chryssostomidis, G.E. Karniadakis, A phase-field method for 3D simulation of two-phase heat transfer, Int. J. Heat Mass Transf. 82 (2015) 282–298.
[33] F. Xie, X. Zheng, M.S. Triantafyllou, Y. Constantinides, Y. Zheng, G.E. Karniadakis, Direct numerical simulations of two-phase flow in an inclined pipe, J. Fluid Mech. 825 (2017) 189–207.
[34] G.E. Karniadakis, Spectral element-Fourier methods for incompressible turbulent flows, Comput. Methods Appl. Mech. Eng. 80 (1990) 367–380.
[35] R.J. Leveque, High-resolution conservative algorithms for advection in incompressible flow, SIAM J. Numer. Anal. 33 (1996) 627–665.
[36] K. Luo, C. Shao, Y. Yang, J. Fan, A mass conserving level set method for detailed numerical simulation of liquid atomization, J. Comput. Phys. 298 (2015) 495–519.
[37] A. Kawano, A simple volume-of-fluid reconstruction method for three-dimensional two-phase flows, Comput. Fluids 134–145 (2016) 130–145.
[38] Z. Solomenko, P.D.M. Spelt, L.Ó. Náraigh, P. Alix, Mass conservation and reduction of parasitic interfacial waves in level-set methods for the numerical simulation of two-phase flows: a comparative study, Int. J. Multiph. Flow 95 (2017) 235–256.
[39] T. Frank, Numerical simulation of slug flow regime for an air-water two-phase flow in horizontal pipes, in: The 11th International Topical Meeting on Nuclear Reactor Thermal-Hydraulics, Avignon, France, 2005.
[40] S. Wenzel, S. Czapp, T. Sattelmayer, Numerical investigation of slug flow in a horizontal pipe using a multi-scale two-phase approach to incorporate gas entrainment effects, in: Proceedings of the 24th International Conference on Nuclear Engineering, vol. 4, American Society of Mechanical Engineers, Charlotte, North Carolina, USA, 2016.
[41] M. Lu, Experimental and Computational Study of Two-Phase Slug Flow, Ph.D. thesis, Imperial College London, 2015.
[42] O. Dinaryanto, Y.A.K. Prayitno, A.I. Majid, A.Z. Hudaya, Y.A. Nusirwan, A. Widyaparaga, Indarto Deendarlianto, Experimental investigation on the initiation and flow development of gas-liquid slug two-phase flow in a horizontal pipe, Exp. Therm. Fluid Sci. 81 (2017) 93–107.
[43] Z.I. Al-Hashimy, H.H. Al-Kayiem, R.W. Time, Z.K. Kadhim, Numerical characterisation of slug flow in horizontal air/water pipe flow, Int. J. Comput. Methods Exp. Meas. 4 (2016) 114–130.
[44] P. Yue, J.J. Feng, C. Liu, J. Shen, A diffuse-interface method for simulating two-phase flows of complex fluids, J. Fluid Mech. 515 (2006) 293–317.
[45] Y. Taitel, A.E. Dukler, A model for predicting flow regime transitions in horizontal and near horizontal gas-liquid flow, AIChE J. 22 (1976) 47–54.
[46] F. Magaletti, F. Picano, M. Chinappi, L. Marino, C.M. Casciola, The sharp-interface limit of the Cahn-Hilliard/Navier-Stokes model for binary fluids, J. Fluid Mech. 714 (2013) 95–126.
[47] D. Jacqmin, Calculation of two-phase Navier–Stokes flows using phase-field modeling, J. Comput. Phys. 155 (1999) 96–127.
[48] H. Abels, D. Lengeler, On sharp interface limits for diffuse interface models for two-phase flows, Interfaces Free Bound. (2014) 395–418.
[49] H. Abels, Y. Liu, A. Schöttl, Sharp interface limits for diffuse interface models for two-phase flows of viscous incompressible fluids, in: D. Bothe, A. Reusken (Eds.), Transport Processes at Fluidic Interfaces, Advances in Mathematical Fluid Mechanics, chap. 9, Springer, Cham, 2017, pp. 231–253.
[50] A.E. Dukler, M.G. Hubbard, A model for gas-liquid slug flow in horizontal and near horizontal tubes, Ind. Eng. Chem. Fundam. 14 (1975) 337–347.
[51] W.P. Jepson, Modelling the transition to slug flow in horizontal conduit, Can. J. Chem. Eng. 67 (1989) 731–740.
[52] P.M. Ujang, C.J. Lawrence, C.P. Hale, G.F. Hewitt, Slug initiation and evolution in two-phase horizontal flow, Int. J. Multiph. Flow 32 (2006) 527–552.
[53] I.T. Ali, CFD Prediction of Stratified and Intermittent Gas-Liquid Two-Phase Turbulent Pipe Flow Using RANS Models, Ph.D. thesis, University of Manchester, 2017.
[54] O.J. Nydal, S. Pintus, P. Andreussi, Statistical characterization of slug flow in horizontal pipes, Int. J. Multiph. Flow 3 (1992) 439–453.